

Cite this: DOI: 00.0000/xxxxxxxxxx

Received Date
Accepted Date

DOI: 00.0000/xxxxxxxxxx

Dynamics and Clogging of colloidal monolayers magnetically driven through an heterogeneous landscape[†]

Sergio Granados Leyva,^a Ralph Lukas Stoop,^a Pietro Tierno,^{a,b,c} and Ignacio Pagonabarraga^{*a,b,d}

We combine experiments and numerical simulations to investigate the emergence of clogging in a system of interacting paramagnetic colloidal particles driven against a disordered landscape of larger obstacles. We consider a single aperture in a landscape of immobile silica particles which are irreversibly attached to the substrate. We use an external rotating magnetic field to generate a traveling wave potential which drives the magnetic particles against these obstacles at a constant and frequency tunable speed. Experimentally we find that the particles display an intermittent dynamics with power law distributions at high frequencies. We reproduce these results by using numerical simulations and shows that clogging in our system arises at large frequency, when the particles desynchronize with the moving landscape. Further, we use the model to explore the hidden role of flexibility in the obstacle displacements and the effect of hydrodynamic interactions between the particles. We also consider numerically the situation of a straight wall and investigate the range of parameters where clogging emerges in such case. Our work provides a soft matter test-bed system to investigate the effect of clogging in driven microscale matter.

Introduction

Understanding the transport properties of microscopic particles through heterogeneous media^{1,2} is important for several technological processes, including filtration,^{3,4} particle sorting,^{5,6} microfluidics^{7,8} and many others across material and engineering science. From a fundamental point of view, there are several fascinating nonequilibrium phenomena that emerge when such particles are driven across disordered landscapes such as depinning, jamming, plastic flow and rectification effects.⁹ These phenomena are also common to other physical systems across different length scales, from vortex matter driven across type II superconductors,¹⁰ to electrons on liquid helium,¹¹ active matter^{12,13} and skyrmions.¹⁴ The simple case of an ensemble of particles forced to pass through a single constriction may give rise to different complex effects, such as intermittency in particle flow, clogging and complete blockage via formation of arches and particle

bridges.¹⁵ This effect has been investigated in the past on different length scales,¹⁶ from humans,¹⁷ to sheeps,¹⁸ granular particles^{19,20} and biological systems.^{21–23} While most of the work has focused on clogging in macroscopic systems, only few studies have addressed the case of microscopic particles dispersed in fluid media.^{16,24,25} At such scale the presence of thermal fluctuation and hydrodynamic interactions between the particles may alter the system dynamics reducing or favoring the effect of clogging.

In this context, some of us²⁶ investigated recently the collective dynamics of paramagnetic colloidal particles that were driven across a disordered landscape of obstacles, namely non magnetic particles fixed at random positions above a surface. While this work focused on the global transport properties in the presence of several obstacles, it did not include the detailed study of a single aperture, where the particle flow is not perturbed by the presence of several openings. Moreover, investigating a single aperture could provide many insight toward understanding the occurrence of clogging in microscale matter, and has a direct connection to the other systems previously mentioned. Thus, in this work, we investigate clogging of colloidal particles when they are forced to pass through a single, narrow opening. Starting from our experimental system, we demonstrate the occurrence of clogging, characterized by a power-law decay of the statistical distribution of the passage time of the particles. We complement our experimental findings with Brownian dynamic simulations which

^a Departament de Física de la Matèria Condensada, Universitat de Barcelona, Av. Diagonal 647, 08028, Barcelona, Spain. Tel: +34 934034031; E-mail: ptierno@ub.edu

^b Universitat de Barcelona Institute of Complex Systems (UBICS), Universitat de Barcelona, Barcelona, Spain.

^c Institut de Nanociència i Nanotecnologia, IN²UB, Universitat de Barcelona, Av. Diagonal 647, 08028, Barcelona, Spain.

^d Centre Européen de Calcul Atomique et Moléculaire, École Polytechnique Fédérale de Lausanne (EPFL), 1015 Lausanne, Switzerland.

[†] Electronic Supplementary Information (ESI) available: two videoclips, one from the experiments and the other from numerical simulation illustrating the dynamics of the driven magnetic colloids. See DOI: 00.0000/00000000.

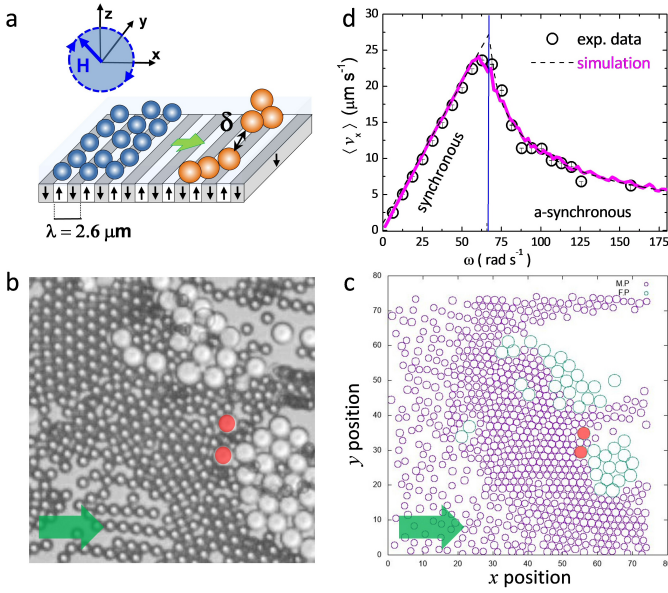


Fig. 1 (a) Schematic showing the experimental system composed of a monolayer of paramagnetic colloids (blue) driven against larger silica particles (orange) and arranged to form one opening of width δ . The particles are located above a ferrite garnet film of wavelength λ and are driven toward right by a rotating magnetic field elliptically polarized in the (\hat{x}, \hat{z}) plane. (b,c) Experimental (b) and simulation (c) images showing a portion of the whole system where the silica particles (larger colloids) form a constriction of width δ . The direction of motion is indicated by a green arrow. See VideoS1 and Video S2 in the Supporting Informations. (d) Mean particle speed $\langle v_x \rangle$ along the direction of motion versus angular frequency ω in the absence of obstacles. Scattered circles are experimental data, while continuous magenta line are results from numerical simulation. The continuous blue line at $\omega_c = 68.8 \text{ rad s}^{-1}$ separates the synchronous (left) and the asynchronous (right) regimes. Dashed lines are fit following the equations in the text.

unveil relevant mechanisms that determine the anomalous flow of the forced colloids, in particular analyzing the role of hydrodynamic interactions and the flexibility of the obstacles at the opening. Finally, we extend the numerical simulations to consider also the situation of a narrow opening in a planar wall of non magnetic particles. While such case is difficult to realize experimentally via direct particle sedimentation, it is similar to many other situations present in e.g. microfluidics systems, which are characterized by fixed and straight PDMS channels.

Methods

Experimental system

We use commercially available paramagnetic colloidal particles (Dynabeads, M-270, Dynal) characterized by a diameter of $d = 2.8 \mu\text{m}$ and a magnetic volume susceptibility of $\chi \sim 0.4$. The particles are composed of a polystyrene matrix with surface carboxylic groups, and are doped with nanoscale iron oxide grains. The particles are dispersed in highly deionized water (MilliQ, Millipore) and deposited above the surface of a uniaxial ferrite garnet film (FGF). The FGF was previously synthesized via dipping liquid phase epitaxy²⁷ and it is characterized by parallel stripes of ferromagnetic domains with alternating up and down magne-

tization. In the absence of an external field, the wavelength of the FGF pattern is $\lambda = 2.6 \mu\text{m}$, and the saturation magnetization $M_s = 1.3 \cdot 10^4 \text{ Am}^{-1}$, see Fig. 1(a). Before the experiments, the FGF is coated with a thin layer ($\sim 1 \mu\text{m}$ thick) of a photoresist (AZ-1512 Microchem, Newton, MA) using spin coating and backing procedures.²⁸

The particles are transported against fixed obstacles made of silica dioxide microspheres (44054-5ML-F, Sigma-Aldrich) with diameter $d = 5 \mu\text{m}$ (standard deviation $\sigma \lesssim 0.35 \mu\text{m}$). Before the experiments, the silica particles are irreversibly attached above the FGF surface with the following procedure. First, the silica particles are diluted in highly deionized water at different concentrations and deposited above the FGF surface. After their sedimentation which lasts few minutes, the particles float above the FGF due to their negative surface charge. Sticking on the substrate is induced by the addition of a salt, namely a solution of 10mM NaCl in water. The NaCl ions of the salt screen the electrostatic interactions favoring permanent linkage of the silica particles to the FGF via attractive van der Waals interactions. After that, the salt solution was removed and was replaced by a water dispersion containing the paramagnetic colloids. As a result, the magnetic particles float on a substrate composed of a quenched disorder of silica obstacles, Fig. 1(b).

Transport mechanism

We start by describing the particle motion in the absence of obstacles. Once placed above the FGF surface, the particles are attracted by the magnetic domain walls, and form a two-dimensional monolayer above the (\hat{x}, \hat{y}) plane. We induce directed particle transport by using an external rotating magnetic field elliptically polarized in a perpendicular plane (\hat{x}, \hat{z}) , see Fig. 1(a). The applied field, with amplitude H_0 and angular frequency ω is given by, $\mathbf{H} = (H_x \cos(\omega t)\hat{x}, 0, H_z \sin(\omega t)\hat{z})$, where $H_0 = \sqrt{(H_x^2 + H_z^2)}/2$, and (H_x, H_z) are the two field components. Since the field is elliptically polarized, it can be characterized also by the ellipticity $\beta = (H_x^2 - H_z^2)/(H_x^2 + H_z^2)$, where $\beta \in [-1, 1]$ and $\beta = 0$ corresponds to the circular polarization. For all the experiments we keep fixed the amplitude to $H_0 = 800 \text{ Am}^{-1}$ and the ellipticity parameter to $\beta = -0.4$. The latter choice ensures that dipolar interactions are negligible along the propulsion direction²⁹ and the particles can be considered, in first approximation, as hard-spheres.

The external magnetic field modulates the stray field of the FGF surface, and it generates a two-dimensional sinusoidal-like potential which continuously translates along one direction (\hat{x}) perpendicular to the magnetic stripes. The potential moves at a constant and frequency tunable speed $v_p = \omega\lambda/(2\pi)$, and drags the paramagnetic colloids located in its minima with it. As shown in Fig. 1(d), depending on the driving frequency one can identify two dynamic regimes.³⁰ Below a critical frequency ω_c , the particles are trapped in the potential minima and move with these minima (synchronous regime) at a constant average speed $\langle v_x \rangle = v_p$. When $\omega > \omega_c$, the motion of the particles desynchronizes with the moving landscape, and the average speed decreases as $\langle v_x \rangle = v_p(1 - \sqrt{1 - (\omega_c/\omega)^2})$ (asynchronous regime).

As shown in Fig. 1(d), we find $\omega_c = 68.8 \text{ rad s}^{-1}$ for the experimental parameters used here, a value which is in excellent agreement with the numerical simulations (see later) for an obstacle free system. Further, in the synchronous regime the particles acquire a translational speed $\langle v_x \rangle \in [2, 23] \mu\text{m s}^{-1}$ which corresponds to a Péclet number $Pe \in [20, 230]$. We estimate the latter by considering the ratio between the Brownian time $\tau_B = d^2/(4D_{eff})$ required by the particle to diffuse its own radius ($d/2$), and the driven time $\tau_D = d/(2\langle v_x \rangle)$ required to move its radius due to the magnetic landscape. Here we use the value of the effective diffusion coefficient $D_{eff} = 0.14 \mu\text{m}^2 \text{s}^{-1}$ which was estimated in a previous work³¹.

Simulation scheme

We complement the experimental results by using Brownian dynamic simulation with periodic boundary conditions. We consider a system composed of moving paramagnetic colloids, of size r_p , and silica obstacles, of size r_o . All particles are characterized by their positions, \mathbf{r}_i with $i = 1 \dots N_p + N_o$. Initially, we consider obstacles fixed on the substrate, $\mathbf{r}_i = \mathbf{r}_{i,eq}$, $i = N_p, \dots, N_p + N_o$, while the magnetic particles evolve following the overdamped dynamics:

$$\frac{1}{\mu} \frac{d\mathbf{r}_i}{dt} = \sum_j \mathbf{F}^{int}(\mathbf{r}_{ij}) + \mathbf{F}^{ext}(\mathbf{r}_i) + \mathbf{F}^T(\mathbf{r}_i), \quad (1)$$

where $i = 1, \dots, N_p$, μ is the particle mobility, \mathbf{F}^{int} is the pair interaction between the colloids, \mathbf{F}^{ext} the external driving force and \mathbf{F}^T accounts for the force exerted by the thermal bath. The interparticle forces derive from a Yukawa potential, and account effectively for the colloidal electrostatic short range repulsion and finite particle size. The force between a particle i of type a , of radius r_a , and a particle j of type b , of radius r_b , can be written as:

$$\mathbf{F}^{int}(\mathbf{r}_{ij}) = \frac{U_{ab}}{\lambda_{ab}} \sum_{i \neq j} \left[\frac{\sigma_{ab}}{r_{ij}} \left(\frac{\sigma_{ab}}{r_{ij}} + \frac{\sigma_{ab}}{\lambda_{ab}} e^{-\frac{r_{ij}}{\lambda_{ab}}} \right) - B_{ab} \right] \mathbf{e}_{r_{ij}}, \quad (2)$$

where $\mathbf{e}_{r_{ij}}$ a unit vector along the two considered particles, and $\mathbf{r}_{ij} = \mathbf{r}_i - \mathbf{r}_j$. The parameter U_{ab} quantifies the strength, and λ_{ab} the characteristic decay length, of the Yukawa potential between the interaction of a particle of type a and one of type b , $\sigma_{ab} = (r_a + r_b)/2$ denotes the radius of the interaction between the pair. The parameter B_{ab} is a constant ensuring that the force is zero at the cutoff interaction radius r_c ,

$$B_{ab} = \frac{\sigma_{ab}}{r_c} e^{-\frac{r_c}{\lambda_{ab}}} \left(\frac{\sigma_{ab}}{\lambda_{ab}} + \frac{\sigma_{ab}}{r_c} \right). \quad (3)$$

We neglect the magnetic dipolar interactions since it was previously shown²⁹ that these interactions become negligibly small along the propulsion direction for applied fields with $\beta = -1/3$, similar to our case. The external force results from the magnetically modulated landscape and is given by²⁹

$$\mathbf{F}^{ext}(\mathbf{x}, t) = F_M \left[u_1(t) \sin\left(\frac{2\pi x}{\lambda}\right) - u_2(t) \cos\left(\frac{2\pi x}{\lambda}\right) \right] \hat{\mathbf{x}} \quad (4)$$

where $u_1(\beta, t) = \sqrt{1 + \beta} \cos(\omega t)$, $u_2(\beta, t) = \sqrt{1 - \beta} \cos(\omega t)$ and $F_M = 16H_0 e^{-2\pi z/\lambda} / (\lambda M_s)$ is a prefactor that considers the particle

elevation (z) from the substrate. The last term in Eq. 1 is a random force associated to the temperature. Integration of this term over one time step, Δt , gives a random displacement $\Delta \mathbf{r}^r$ characterized by a Gaussian distribution, of magnitude $\Delta \mathbf{r}^r = \mu \mathbf{F}_i^T \Delta t$ and $\langle (\Delta \mathbf{r}^r)^2 \rangle = 4D_0 \Delta t$, being D_0 the particle diffusion coefficient.

For computational convenience, we make Equation 1 adimensional using the magnitude of the external force F_M , the colloid radius r_p , the characteristic speed $v_c = F_M \mu$ and time $\tau_D = d/2\mu F_M$ scales, which identify the relevant Péclet number, $Pe = v_c r_p / D_0 = \mu F_M \sigma / D_0$. Accordingly, we can rewrite Eq. 1 as:

$$\frac{d\tilde{\mathbf{r}}_i}{dt} = \frac{U_{ab}}{\lambda_{ab} F_M} \sum_{j \neq i} \tilde{\Psi}(\tilde{\mathbf{r}}_{ij}) + \tilde{\mathbf{F}}^{ext}(\tilde{\mathbf{x}}, \tilde{t}) + \sqrt{\frac{4}{Pe} \frac{\tau_D}{\Delta t}} \tilde{\xi} \quad (5)$$

where $\tilde{\mathbf{r}} = \mathbf{r}/r_p$, $\tilde{\omega} = \omega \tau_D$, $\tilde{\Delta t} = \Delta t/\tau_p$. In turn, $\tilde{\Psi} = \tilde{\Psi}(\tilde{\mathbf{r}})_{ij}$ is the dimensionless Yukawa force between particles i and j ,

$$\tilde{\Psi}(\tilde{\mathbf{r}}_{ij}) = \left[\frac{\tilde{\sigma}_{ab}}{\tilde{r}_{ij}} \left(\frac{\tilde{\sigma}_{ab}}{\tilde{r}_{ij}} + \frac{\tilde{\sigma}_{ab}}{\tilde{\lambda}_{ab}} e^{-\frac{\tilde{r}_{ij}}{\tilde{\lambda}_{ab}}} \right) - B_{ab} \right] \mathbf{e}_{r_{ij}} \quad (6)$$

where $\tilde{\sigma}_{ab} = \sigma_{ab}/r_p$, and $\tilde{\lambda}_{ab} = \lambda_{ab}/r_p$. Finally, $\tilde{\mathbf{F}}^{ext}(\tilde{\mathbf{x}}, \tilde{t})$ corresponds to the dimensionless form of the external, driving force, Eq. 4.

We integrate Eq. 5 using a time step $\Delta t/\tau_D = 1 \cdot 10^{-4}$, $r_p = 1$, $r_o = 1.78$, $\lambda_p = 1$, $\lambda_{op} = 1.39$, $U_{pp}/\lambda_{pp} F_M = 300$, $U_{op}/\lambda_{op} F_M = 150$ and $Pe = 150$. Further parameters were extracted by fitting the results from the experimental data to the one obtained from numerical simulation of an obstacle free system, see Fig. 1(d). From this benchmarking, we estimate the mobility $\mu \simeq 1/6\pi\eta r_a$ of the paramagnetic particles in water as $\mu = 3.79 \cdot 10^7 \text{ N s m}^{-1}$ and the magnitude of the force of the traveling wave potential as $F_M = 0.1 \text{ pN}$. With these values we calculate the characteristic time of the particle motion as $\tau_D = 0.04 \text{ s}$. Having demonstrated a good agreement between the simulations and the experiments in the absence of obstacles, we introduce the obstacles to our simulations. As shown in Fig. 1(c), we map the experimental situation (Fig. 1(b)) to our simulations by using the same spatial distribution of the obstacles.

In the numerical simulations obstacles are considered as rigidly attached to the substrate, and N then runs only over paramagnetic colloids. Careful inspection of the experimental videos reveals very small oscillations of the silica particles around their equilibrium position upon collisions. These oscillations may result from a combination between steric interactions of the silica particles with the polymer coated film and weak Van der Waals attractions. Quantifying these interactions is a difficult task, and we consider them as an effective spring constant which accounts for the fact that the silica particles are not pulled away when subjected to forces coming from the driven colloids. Moreover, these oscillations are very small, and their amplitude is smaller than the error bars associated to the tracking. To account for this effect, we take into account the possibility that the obstacles are slightly displaced due to the forces exerted by the moving paramagnetic colloids. In this case we include the obstacles as part of the N

moving particles, which evolve according to the equation:

$$\frac{d\tilde{\mathbf{r}}_i}{dt} = \sum_{j \neq i} \frac{U_{ab}}{\lambda_{ab} F_M \mu} \tilde{\Psi}(\tilde{\mathbf{r}}_{ij}) + \frac{k r_p}{\mu F_M} (\tilde{\mathbf{r}}_i - \tilde{\mathbf{r}}_{i,eq}), \quad (7)$$

with $i = N_p + 1, \dots, N_p + N_o$. The particles are subject to a spring of strength k whenever the obstacle is displaced from its equilibrium position, $\tilde{\mathbf{r}}_{i,eq}$. The competition between the external driving frequency and the one related with the elastically displaced particles can lead to different and significant results.

Since the colloids are embedded in a solvent, we have also generalized the Brownian dynamics of the paramagnetic colloids to accounts for the impact that hydrodynamic interactions mediated by the solvent has in the clogging kinetics. Each particle is dragged by the fluid flow, \mathbf{v}_i^H , generated by the rest of the colloids due to the forces they are subject to, an effect that can be captured generalizing eq.(1) to

$$\frac{1}{\mu} \frac{d\mathbf{r}_i}{dt} = \sum_j \mathbf{F}^{int}(\mathbf{r}_{ij}) + \mathbf{F}^{ext}(\mathbf{r}_i) + \mathbf{F}^T(\mathbf{r}_i) + \frac{\mathbf{v}_i^H}{\mu}, \quad (8)$$

where we take into account the impact that the close proximity of the wall, and express the induced velocity in the point particle approximation as:

$$\mathbf{v}_i^H = \sum_{j \neq i} \mathbf{G}(\mathbf{r}_{ij}) \mathbf{F}^{int}(\mathbf{r}_{ij}). \quad (9)$$

Here where $\mathbf{G}(\mathbf{r}_{ij})$ stands for the Blake-Oseen mobility tensor³² which considers the effect of the close proximity of the substrate in a far field approximation. We note that a sample with finite size could produce a screening of the hydrodynamic interactions between the particles. However, in our case the experimental cell is wide enough that this screening develops over length scales that are long compared with the distances over which the particles interact and move through the obstacles.

Discussion

Clogging: experimental results

Introducing obstacles to the substrate completely changes the behavior of the driven particles as they are now forced to interact with the silica spheres which induces a deviation of their trajectories. As shown in Figs. 1(c,d), we consider the case of obstacles which create a narrow gap of width δ . We find that the presence of the opening strongly reduces the average speed of the monolayer eventually even leading to complete blockage, $\langle v_x \rangle = 0$, for $\delta < 3\mu\text{m}$. For larger values of the distance $3\mu\text{m} < \delta < 4\mu\text{m}$, we find an intermittent flow of the magnetic colloids which arises from the simultaneous arrival of the particles at the aperture, and their accumulation in a close packed state, which is locally jammed.

The appearance of clogging, namely the blockage of the particle flow, can be characterized by measuring the distribution $P(t_p)$ that quantifies when the time lapse between the passage of consecutive particles through the aperture is larger than a given time t_p . This distribution is also known as the complementary cumulative distribution function. It has been previously shown that in

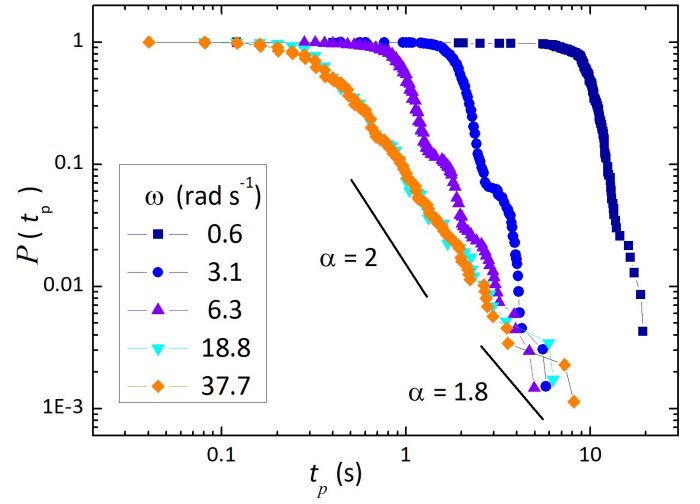


Fig. 2 Experiments: The distribution function $P(t_p)$ of time lapses $t > t_p$ for magnetic particles passing through a single constriction and at different driving frequencies. The continuous black line indicates the slope $\alpha = 2$ of the power-law $P \sim t_p^{-\alpha}$ which is used to distinguish clogged state ($\alpha < 2$) and unclogged ones ($\alpha > 2$).

the presence of an intermittent flow such distribution is expected to display asymptotically an universal behavior, i.e. a power law decay at high values of t_p ($P \sim t_p^{-\alpha}$) as a function of its exponent, α .^{19,33} This exponent can be used to distinguish the regime of normal flow, $\alpha > 2$, i. e. when the average flow rate is finite, from intermittency and clogging, $\alpha < 2$, i. e. when the average time lapse between consecutive passing elements trough the aperture diverges. Hence, we can use $\alpha = 2$ to identify the transition to clogging, where it cannot be specified whether or not there is flow at a give time.¹⁶ Indeed a clogged state it is not fully blocked, as some material can be briefly released.

We use video microscopy to precisely track the positions of the particles and to calculate the corresponding distributions. Fig. 2 shows $P(t_p)$ measured for different values of the driving frequency ω and keeping constant the amplitude of the applied field. We find two different types of behaviour depending on ω which reflect the presence in the system of the underlying magnetic domain walls. For small frequencies, namely $\omega < 6.3 \text{ rad s}^{-1}$, clogging events are rare, and the distribution P displays an exponential decay. This effect can be understood by considering particle trajectories which are characterized by a sequence of discrete jumps between the domain walls during each driving period. These jumps emerge in the system as periodic oscillations of the particles which are superimposed to the net drift velocity. The presence of such vibrations significantly reduces the clogging probability and the eventual formation of particle bridges. Such effect can be considered as an additional AC signal superimposed to the DC drift and allows to break the formation of a close packed monolayer of particles close to the constriction.¹⁹ We note that a similar strategy, namely the use of an additional AC field to fluidized the system, was recently introduced in numerical simulation to maximize flow in a random obstacle array.²³ In contrast, at high frequencies, the particles still move across the domain

walls but their trajectories are continuous as the discrete jump are smeared out. As a consequence, the vibrations of the domain walls are not influencing the particle movement and cannot fluidize the system close to the constriction. Thus, we find that P becomes a power law, $P \sim t_p^{-\alpha}$ and the systems is more prone to display clogging behavior. For these situations, we determine a common exponent $\alpha = 1.8$ for the tails of the high frequency distributions.³⁴ Such value is slightly higher as compared to pedestrian or granular systems that display stable arches at the constriction.^{15,20} The specificity of the colloidal system, and the role that the hydrodynamic interactions may have among the relative motion of the colloids close to the constriction may explain that the observed clogged states are more fragile than those observed on systems composed by larger constituents. Moreover, we find that all curves above $\omega = 6.3 \text{ rad s}^{-1}$ collapse, and clogging becomes independent on the particle speed. We note that experimental limitations impeded us to have enough statistical data, and thus to precisely determine the exponent of the distribution tails. Such limitations result from the unavoidable sticking of the particles to the FGF film after relatively long recording periods.

Simulation results: fixed obstacles

Figs. 3(a,b) display the results from the numerical simulations for fixed obstacles. In Fig. 3(a) we show how the distribution function $P(t_p)$ changes by varying the distance between the obstacles forming the constriction, at fixed driving frequency. As expected, a narrower constriction increases the particle mean passing time. Similar to the experimental data, we also observe a periodic decrease of the distributions followed by a series of characteristic plateaus which result from the external sinusoidal forcing. Indeed the time between two consecutive decays is proportional to the period of the applied field, $T = 1/f$. These plateaus are more evident in the simulations than in the experiments (Fig. 2), due to the higher temporal resolution achieved numerically. In the plateaus colloids have a higher probability to pass through the constriction, since they are located in a place where the potential is steeper, and thus feel a maximum positive force along the direction of motion. As the opening associated to a pair of obstacles decreases, these plateaus become narrower and the corresponding distributions smoother. Further, we find that for all the cases considered here, the system never develops a power law decay. Thus, no clogged states are present in the synchronous regime, in contrast to the experimental case where $\alpha = 1.8$ was observed for large ω but still slightly lower than ω_c .

As shown in Fig. 3(b), the free speed of the paramagnetic particles, proportional to the driving frequency ω in the synchronous regime, strongly influences the distribution of t_p . In fact, increasing ω shifts the time lapse distribution towards shorter times, with a decay that may be characterized by an exponential law similar to the experimental results in Fig. 2. Interestingly, this trend reverses after $\omega = 37.7 \text{ rad s}^{-1}$ as the tails of the distributions flatten and become power law but with no signature of clogging, $\alpha > 2$. Above $\omega = 85.7 \text{ rad s}^{-1}$, as the particles reach the asynchronous region, the $P(t_p)$ develop power law tails with $\alpha \sim 1.8$ signaling clogging. This results shows that losing synchrony pro-

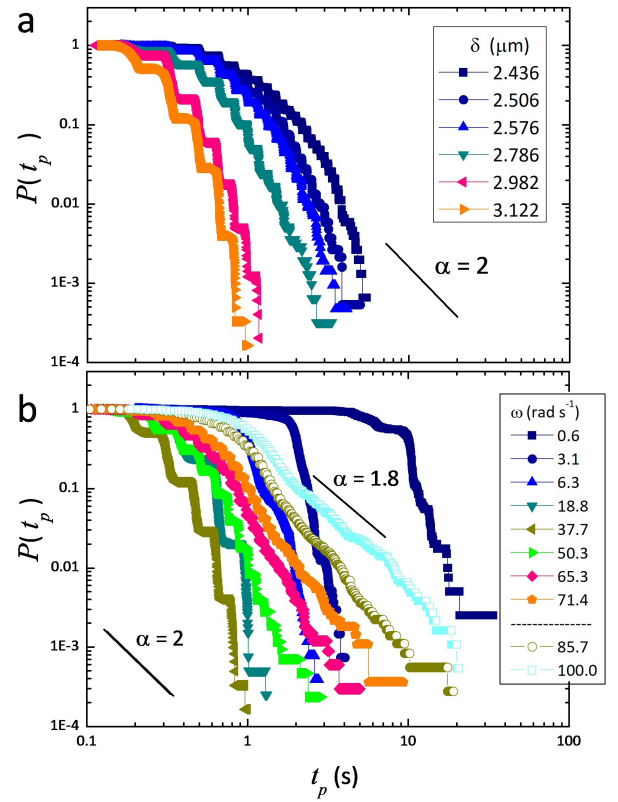


Fig. 3 (a,b) Numerical simulation results in the synchronous regime ($\omega = 37.7 \text{ rad s}^{-1}$). (a) Distribution functions $P(t_p)$ of time lapses t_p for different values of the constriction width δ . (b) Distribution functions $P(t_p)$ of time lapses t_p for different values of driving frequency ω , with $\delta = 2.98 \mu\text{m}$. The results are shown for particles driven in the synchronous regime for $\omega \leq 71.4 \text{ rad s}^{-1}$, and in the asynchronous regime for larger ω .

notes clogging.

Simulation results: Harmonic spring and Hydrodynamic interactions

The results obtained by fixing the positions of the obstacles shows the emergence of clogging at high frequencies, however they did not capture all the effects observed in the experiments as, for example, the collapse of the distributions at high frequencies in the synchronous regime. In order to analyze the origin of such discrepancy, we consider the impact that moving obstacles and the hydrodynamic interactions have on the system dynamics. To this end, we first introduce a small flexibility in the obstacle location and show in Fig. 4(a) the corresponding results. The presence of another vibration frequency resulting from the obstacle mobility can have relevant effects and contribute directly to the effect of clogging. To find the optimal spring constant k , we have performed different simulations and compare them directly with the experimental results in order to optimize the comparison. We find a very similar distribution for a spring constant $k = 0.593 \mu\text{N m}^{-1}$. Moreover, similar to the experiments we also observe the collapse of the distributions at high frequencies by keeping fixed k and varying ω , Fig. 4(a). Thus, the presence of slightly mobile obstacles favors clogging, while using the same constriction width

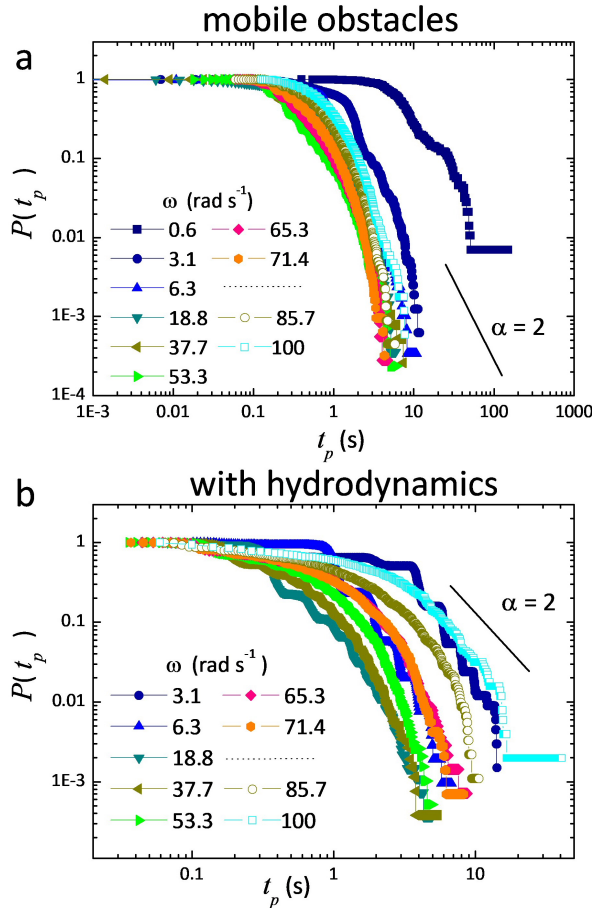


Fig. 4 (a) Distribution functions $P(t_p)$ of time lapses t_p for different values of driving frequency ω both in the synchronous (filled symbols) and asynchronous (empty symbols) regime from numerical simulations. The simulations were performed by considering mobile obstacles with a spring constant $k = 0.593 \mu\text{Nm}^{-1}$. The black segment indicates the slope $\alpha = 2$ of the power law $P \sim t^{-\alpha}$. (b) Distribution functions $P(t_p)$ of time lapses t_p versus ω from the numerical simulations with hydrodynamic interactions. The channel width for all data has been fixed to $\delta = 2.576 \mu\text{m}$.

with no harmonic spring gives a completely unclogged state and a large exponent in the distribution $P(t_p)$, $\alpha > 2$. Further, as shown in Fig. 4(a), we find that there are no visible plateaus as in Fig. 3. Moreover, smaller spring constants can lead to a more clogged state than higher ones. The latter effect is unexpected, as smaller frequencies could induce longer period of time when the obstacle are more deformed and the width of the opening wider, which should favor unclogging. However, the results obtained in Fig. 4(a) point out to an interplay between the frequency of the external magnetic field and the frequency of oscillation of the obstacles which favor clogging, e.g. obstacle mobility leads to an interaction with other constrictions because particles passing through nearby openings, see Fig. 1(b), can also indirectly exert additional pressure on the obstacles of the opening of interest, affecting the colloidal passage times.

Experimentally, the paramagnetic colloids move above the FGF film generating a net flux between them and close to the constriction, see previous section for details. We use the extended Brow-

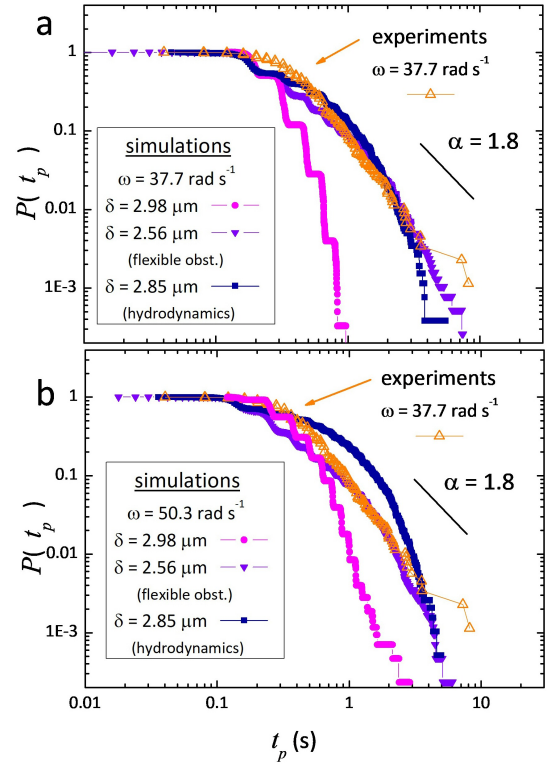


Fig. 5 (a,b) Comparison between the experimental data (open symbols), frequency $\omega = 37.7 \text{ rad s}^{-1}$ and the numerical simulations (filled symbols) driving frequencies: (a) $\omega = 37.7 \text{ rad s}^{-1}$ and (b) $\omega = 50.3 \text{ rad s}^{-1}$. In both images the black segment denotes the slope $\alpha = 1.8$ of the power law $P(t_p)$.

nian Dynamics model described in the Method section to analyze the impact that hydrodynamic interactions (HIs) have in the cumulative colloidal passing times. As shown in Fig. 4(b), we also explore the effect of HIs by varying the driving frequency from the synchronous ($\omega < 85.7 \text{ rad s}^{-1}$) to the a-synchronous regime. The emergence of the finite plateaus is also observed at low frequency, while raising ω smooths the curves and produces power law tails, Fig. 4(b).

The direct comparison with the experimental data taken at $\omega = 37.7 \text{ rad s}^{-1}$ is shown in Figs. 5(a,b) for two frequencies both in the synchronous regime. The numerical simulations show that the introduction both of obstacle mobility and HI smooth significantly the plateaus, to the extent that they are barely visible when HI are introduced with fixed obstacles. Moreover, flexible obstacles induce distribution functions which have dependence with frequency closer to the one observed experimentally.

Simulation results: planar wall

The geometry analyzed in the previous section with numerical simulation was designed to match the experimental system, thus featuring obstacles with the same position and degrees of disorder. Such disorder results from the procedure to prepare the obstacles, since the silica particles were left sediment above the substrate and forced to stick there by addition of salt. Thus,

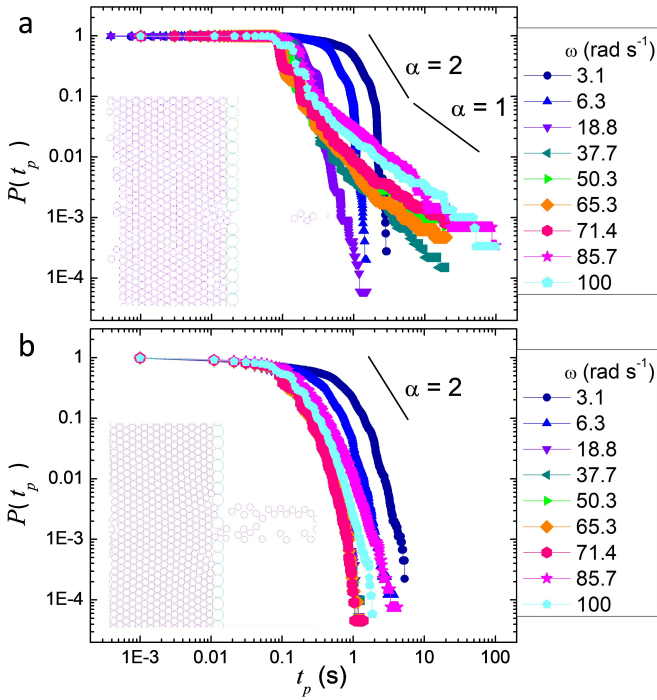


Fig. 6 (a,b) Distribution functions $P(t_p)$ of time lapses, t_p , for different frequencies of a straight wall of non magnetic colloids with: (a) a single constriction with width $\delta = 2.982\mu\text{m}$ and (b), two small constrictions both with width $\delta = 2.982\mu\text{m}$ and separated by a single particle. The small insets on the left of both images show a fraction of the simulation box with a close packed monolayer of particles. The inset at the top show channel clogging, while the inset at the bottom simple particle flow.

adapting the simulation to the experimental system implies a random distribution of the particles and an opening with a small inclination with respect to the driving direction, as shown in Fig. 1(c). However, it is also interesting to analyze the generic features of the probability of elapsed times on a simplified geometry, when the silica obstacles form a perfect planar wall with a small opening at the center. This geometry is depicted in the inset of Fig. 6(a), for a width $\delta = 2.982\mu\text{m}$, while the main figure shows the variation of $P(t_p)$ as a function of ω . At very low frequencies, $\omega < 18.8\text{rad s}^{-1}$, the distributions are exponential and the particles easily flow through the aperture. Increasing ω we observe the emergence of the steps as in the previous case, however we find that clogging may be observed even within the synchronous regime ($\omega = 65.3\text{rad s}^{-1}$) where the power law distributions feature a very small exponent $\alpha \sim 1.2$. The reason is that, in contrast to the disordered geometry, the planar may act as a template for crystallization (see inset Fig. 6(a)) and create arches and bridges which easily impeded further motion, creating an intermittent flow at the opening. In contrast at low frequency the particle oscillations due to the moving landscape are able to break these bridges and to avoid the crystallization process.

Further, the numerical system allows to explore the effect that an additional opening in the straight wall will have on the global particle flow. An interesting question is whether adding a second aperture separated by only one silica obstacle, could favor the

system fluidization and avoid clogging. We effectively report this effect in Fig. 6(b), where two apertures of width $\delta = 2.982\mu\text{m}$ are able to avoid the particle crystallization which induces clogging for all driving frequencies. The measured distribution functions $P(t_p)$ for both apertures are almost identical, and in both cases (in Fig. 6(b) we show their average) display a smooth and almost exponential decay. We note that the effect of two openings may be considered analogous to placing a single obstacle at the exit of one large aperture. This situation has been used in the past in other macroscopic systems as an efficient means to fluidize a system prone to clogging^{35–37}. However, in most cases the obstacle was placed close to the opening, but not exactly at the exit. Another interesting avenue for future study is to investigate how the distributions function may change upon variation of different parameters, such as the location and size of the central obstacle, or when the two opening are asymmetric, namely with different width.

Conclusions

We have studied both experimentally and theoretically the dynamics of paramagnetic colloidal particles driven through a single aperture above a periodic magnetic substrate. We combine experiments with numerical simulations and analyze the distribution of displacements of the particles. We find that in the experiments clogging occurs when the particles are driven close to the asynchronous regime, while in the simulations they always occur deep in this regime. Further we unveil the role played by the obstacle movement due to flexibility and to the hydrodynamic interactions. The comparison between experimental and simulation results on analogous geometries indicate that HI play a relevant role in the clogging dynamics of forced colloids and that obstacle compliance hinders the dependence of particle motion on the frequency of the driving field.

While the experimental system is based on the use of a specially prepared ferrite garnet film, we observe a very good agreement between the experimental data and the results from numerical simulations by using a very generic model. The latter neglect dipolar interactions between the particles while considering an effective short range repulsive interaction potential. Thus our findings may be used to explore clogging in other driven many particle systems two dimensionally confined to a plate, not limited to magnetic ones. On the other hand, the possibility of increasing the dipolar interactions between the particles via the ellipticity of the applied field could be further used as an effective tool to switch on attractive interactions and induce chaining.

Moreover, our findings invite future explorations of the system, as considering two, three or several opening in different geometric arrangements. Another interesting avenue would be to explore how the overall dynamics changes for anisotropic magnetic particles driven through the aperture.^{38–43} On the application side, the possibility of transporting paramagnetic colloidal particles close to a surface, and localize their position by simply switching off the applied field may be of interest for microfluidics⁴⁴ and lab-on-a-chip⁴⁵ systems. In particular, these particles can be used to pick up and mobilize a chemical or biological cargo via surface functionalization⁴⁶.

Conflicts of interest

There are no conflicts to declare.

Acknowledgements

We thank Tom H. Johansen for providing us with the FGF film. R. L. S. acknowledges support from the Swiss National Science Foundation Grant 180729. R. L. S. and P. T. acknowledge support from the ERC consolidator grant Enforce (No. 811234). P. T. acknowledges support from the Ministerio de Ciencia, Innovación y Universidades (Grant no. ERC2018-092827) and the Generalitat de Catalunya (2017SGR1061 and program ICREA Acadèmia). I. P. acknowledges support from Ministerio de Ciencia, Innovación y Universidades (Grant No. PGC2018-098373-B-I00), DURSI (Grant No. 2017 SGR 884), and SNF (Project No. 200021-175719).

Notes and references

- 1 M. B. Isichenko, *Rev. Mod. Phys.*, 1992, **64**, 961–1043.
- 2 A. A. Snarskii, I. V. Bezsudnov, V. A. Sevryukov, A. Morozovskiy and J. Malinsky, *Transport Processes in Macroscopically Disordered Media: From Mean Field Theory to Percolation*, Springer, New York, 2016.
- 3 S. Redner and S. Datta, *Phys. Rev. Lett.*, 2000, **84**, 6018–6021.
- 4 N. Roussel, T. L. H. Nguyen and P. Coussot, *Phys. Rev. Lett.*, 2007, **98**, 114502.
- 5 M. P. MacDonald, G. C. Spalding and K. Dholaki, *Nature*, 2003, **426**, 421.
- 6 F. Martinez-Pedrero, H. Massana-Cid, T. Ziegler, T. H. Johansen, A. V. Straube and P. Tierno, *Phys. Chem. Chem. Phys.*, 2016, **18**, 26353.
- 7 T. M. Squires and S. R. Quake, *Rev. Mod. Phys.*, 2005, **77**, 977–1026.
- 8 G. Whitesides, *Nature*, 2006, **442**, 368–373.
- 9 C. Reichhardt and C. J. O. Reichhardt, *Rep. Prog. Phys.*, 2017, **80**, 026501.
- 10 L. F. Cohen and H. J. Jensen, *Rep. Prog. Phys.*, 1997, **60**, 1581.
- 11 D. G. Rees, H. Totsuji and K. Kono, *Phys. Rev. Lett.*, 2012, **108**, 176801.
- 12 C. Bechinger, R. Di Leonardo, H. Löwen, C. Reichhardt, G. Volpe and G. Volpe, *Rev. Mod. Phys.*, 2016, **88**, 045006.
- 13 D. R. Parisi, R. C. Hidalgo and I. Zuriguel, *Scientific Reports*, 2018, **8**, 9133.
- 14 C. Reichhardt, D. Ray and C. J. O. Reichhardt, *Phys. Rev. Lett.*, 2015, **114**, 217202.
- 15 C. Lozano, G. Lumay, I. Zuriguel, R. C. Hidalgo and A. Garcimartín, *Phys. Rev. Lett.*, 2012, **109**, 068001.
- 16 I. Zuriguel, D. R. Parisi, R. C. Hidalgo, C. Lozano, A. Janda, P. A. Gago, J. P. Peralta, L. M. Ferrer, L. A. Pugnaroni, E. Clément, D. Maza, I. Pagonabarraga and A. Garcimartín, *Scientific Reports*, 2015, **4**, 7324.
- 17 D. Helbing and P. Molnár, *Phys. Rev. E*, 1995, **51**, 4282–4286.
- 18 A. Garcimartín, J. M. Pastor, L. M. Ferrer, J. J. Ramos, C. Martín-Gómez and I. Zuriguel, *Phys. Rev. E*, 2015, **91**, 022808.
- 19 A. Janda, D. Maza, A. Garcimartín, E. Kolb, J. Lanuza and E. Clément, *Europhys. Lett.*, 2009, **87**, 24002.
- 20 K. To, P.-Y. Lai and H. K. Pak, *Phys. Rev. Lett.*, 2001, **86**, 71–74.
- 21 P. Galajda, J. Keymer, P. Chaikin and R. Austin, *Journal of Bacteriology*, 2007, **189**, 8704–8707.
- 22 N. Koumakis, A. Lepore, C. Maggi and R. Di Leonardo, *Nat. Comm.*, 2013, **4**, 2588.
- 23 C. Reichhardt and C. J. O. Reichhardt, *Phys. Rev. Lett.*, 2018, **121**, 068001.
- 24 M. D. Haw, *Phys. Rev. Lett.*, 2004, **92**, 185506.
- 25 A. Marin, H. Lhuissier, M. Rossi and C. J. Kähler, *Phys. Rev. E*, 2018, **97**, 021102.
- 26 R. L. Stoop and P. Tierno, *Communications Phys.*, 2018, **1**, 68.
- 27 P. Tierno, F. Sagués, T. H. Johansen and T. M. Fischer, *Phys. Chem. Chem. Phys.*, 2009, **11**, 9615–9625.
- 28 P. Tierno, *Phys. Rev. Lett.*, 2012, **109**, 198304.
- 29 A. V. Straube and P. Tierno, *Soft Matter*, 2014, **10**, 3915.
- 30 A. V. Straube and P. Tierno, *Europhys. Lett.*, 2013, **103**, 28001.
- 31 P. Tierno, R. Muruganathan and T. M. Fischer, *Phys. Rev. Lett.*, 2007, **98**, 028301.
- 32 J. R. Blake and A. T. J. Chwang, *Eng Math*, 1974, **8**, 23.
- 33 C. Saloma, G. J. Perez, G. Tapang, M. Lim and C. Palmes-Saloma, *Proc. Nat. Acad. Sci. USA*, 2003, **100**, 11947.
- 34 A. Clauset, C. R. Shalizi and M. E. J. Newman, *SIAM review*, 2009, **51**, 661.
- 35 I. Zuriguel, A. Janda, A. Garcimartín, C. Lozano, R. Arévalo and D. Maza, *Phys. Rev. Lett.*, 2011, **107**, 278001.
- 36 K. Endo, K. A. Reddy and H. Katsuragi, *Phys. Rev. Fluids*, 2017, **2**, 094302.
- 37 M. G. Areán, A. Boschan, M. A. Cachile and M. A. Aguirre, *Phys. Rev. E*, 2020, **101**, 022901.
- 38 D. Zerrouki, J. Baudry, D. Pine, P. Chaikin and J. Bibette, *Nature*, 2008, **455**, 380.
- 39 L. S. H. and L. C. M., *Small*, 2009, **5**, 1957.
- 40 J. Yan, M. Bloom, S. C. Bae, L. E. and S. Granick, *Nature*, 2012, **491**, 578.
- 41 J. Palacci, S. Sacanna, A. Vatchinsky, P. M. Chaikin and D. J. Pine, *J. Am. Chem. Soc.*, 2013, **135**, 15978.
- 42 P. Tierno, *Phys. Chem. Chem. Phys.*, 2014, **16**, 23515.
- 43 F. Martinez-Pedrero, E. Navarro-Argemí, A. Ortiz-Ambriz, I. Pagonabarraga and P. Tierno, *Science Adv.*, 2018, **4**, 9379.
- 44 A. Terray, J. Oakey and D. W. Marr, *Science*, 2002, **296**, 1841.
- 45 L. Wang, M. Zhang, J. Li, X. Gong and W. Wen, *Lab chip*, 2010, **10**, 2869.
- 46 T. Garg, G. Rath and A. K. Goyal, *Crit. Rev. Ther. Drug Carrier Syst.*, 2015, **32**, 89.